

Mechanistic benefits of millisecond annealing for diffusion and activation of boron in silicon

Charlotte T. M. Kwok,¹ Richard D. Braatz,¹ Silke Paul,² Wilfried Lerch,² and Edmund G. Seebauer^{1,a)}

¹*Department of Chemical and Biomolecular Engineering, University of Illinois, Urbana, Illinois 61801, USA*

²*Mattson Thermal Products GmbH, Daimlerstrasse 10, 89160 Dornstadt, Germany*

(Received 17 October 2008; accepted 5 January 2009; published online 19 March 2009)

Millisecond annealing techniques with flash lamps or lasers have become increasingly common for activating dopants and eliminating implantation-induced damage after ion implantation for transistor junction formation in silicon. Empirical data show that such techniques confer significant benefits, but key physical mechanisms underlying these benefits are not well understood. The present work employs numerical simulation and analytical modeling to show that for boron, millisecond annealing reduces unwanted dopant spreading by greatly reducing the time for diffusion, which more than compensates for an increased concentration of Si interstitials that promote dopant spreading. Millisecond annealing also favorably alters the relative balance of boron interstitial sequestration by the crystal lattice vs interstitial clusters, which leads to improved electrical activation at depths just short of the junction. © 2009 American Institute of Physics.

[DOI: [10.1063/1.3079524](https://doi.org/10.1063/1.3079524)]

I. INTRODUCTION

The continual shrinking of transistor size in silicon-based integrated circuit fabrication technologies has imposed increasingly stringent requirements on *pn* junction properties such as junction depth, profile abruptness, and sheet resistance.¹ The need to incorporate high concentrations of electrically active dopant within 20 nm or less of the surface poses difficult challenges for ion implantation technology and subsequent thermal annealing. Annealing methodology has progressed over the past decade toward faster ramp rates and shorter high-temperature cycle times—from roughly 1 s in rapid thermal processing (RTP) (Ref. 2) to roughly 1 ms or less in flash³ and laser annealing.³ This progression has led to less dopant diffusion and improved electrical activation, especially in the problematic case of boron. However, key physical mechanisms underlying these benefits are not well understood. Moreover, the relative merits of combining different annealing programs, such as flash-assist rapid thermal processing (fRTP) (Ref. 4) or furnace annealing followed by laser irradiation,³ also lack clear physical explanation. Progress has been made largely on an empirical basis. The present work uses a combination of numerical simulation and analytical modeling to develop a physical picture that explains the origin of the benefits conferred by millisecond annealing of boron implanted into silicon.

Numerical simulations have long been used to quantify the effects of annealing on the elementary kinetic steps that compose the boron diffusion/reaction network. However, the network contains so many steps and is so complicated that a focused physical understanding of key phenomena is difficult to discern based solely upon simulation results. A complete

kinetic description that incorporates all reacting species (such as interstitial clusters of many sizes and stoichiometries) leads to a model containing many dozens of activation energies and pre-exponential factors, most of which cannot be measured directly or obtained reliably from quantum calculations. The parameters within such a simulation model are therefore typically obtained via fitting large experimental data sets together with making artful presuppositions about the reasonability of the parameters. Such an approach can yield accurate correlation models within the domain of experimental data but casts doubt upon subsequent physical interpretation.

Some recent work has pursued a different approach that simplifies the kinetic description by dramatically reducing the number of rate equations but simultaneously choosing the remaining equations to capture the key elements of a restricted set of phenomena. Corresponding rate parameters are estimated through Bayesian statistics. For example, descriptions have emerged⁵ that incorporate a more accurate description of interstitials via surface dangling bonds^{6,7} and the effects of near-surface band bending.⁸ The present work employs such an approach for boron. Simulations are employed to estimate the spatial and temporal variation in boron and silicon interstitial atoms during spike and flash annealing, and those values are subsequently incorporated into easily interpreted analytical kinetic expressions that describe the salient features of dopant diffusion and activation.

II. EXPERIMENTAL METHODS

To develop the simulation model for use over an adequately broad set of annealing regimes, a kinetic parameter set was developed from experimental data for the diffusion and activation of implanted boron via three standard protocols: soak annealing over many minutes, spike annealing of

^{a)}Author to whom correspondence should be addressed. Electronic mail: eseebaue@uiuc.edu.

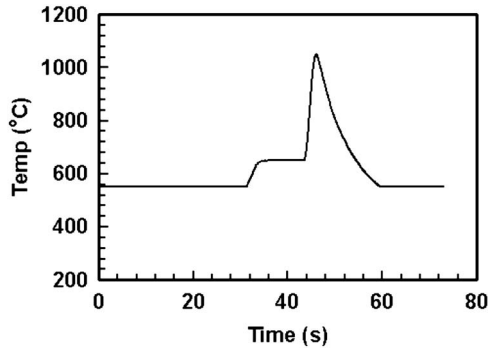


FIG. 1. Temperature trajectory for spike annealing with a peak temperature of 1050 °C.

about 1 s, and millisecond (flash) annealing of about 1 ms. Details of experimental methods for soak and spike annealing have already been detailed in Ref. 5, but the key features were as follows. For soak annealing, *n*-type Si(100) specimens about 1.5 cm × 1 cm implanted with boron at 2 keV and a dose of 1×10^{15} ions/cm² were cut from conventional wafers and mounted between Ta clips for resistive heating. Heating was performed^{9,10} in a turbomolecularly pumped high vacuum chamber with a working pressure in the low 10^{-8} torr range. Samples were annealed at 900 °C for 1 h. Spike and flash annealing⁴ employed *n*-type Si (100) wafers implanted with boron at 0.5 keV with a dose of 1×10^{15} ions/cm². Before implantation, the native oxide was removed by wet-chemical etching in HF (49%):H₂O solution. Spike annealing was performed in a Mattson RTP system with a maximum temperature of 1000 °C–1050 °C. Flash annealing was performed with a peak temperature of 1256 °C–1322 °C. Typical temperature programs for spike and flash annealing are shown in Figs. 1 and 2, respectively. The gaseous ambient for both spike and flash annealing was N₂ at 1 atm incorporating 100 ppm partial pressure of O₂.

Characterization of soak-annealed samples was performed at the University of Illinois. Concentration profiles were measured *ex situ* by secondary ion mass spectroscopy (SIMS) using a CAMECA IMS-5f instrument. Sheet resistance was measured by a standard four-point probe. The spike and flash annealed samples were analyzed at Mattson, with profiles measured *ex situ* by SIMS on a FEI SIMS 4600 quadrupole depth profiler. For dopant activation, full-wafer

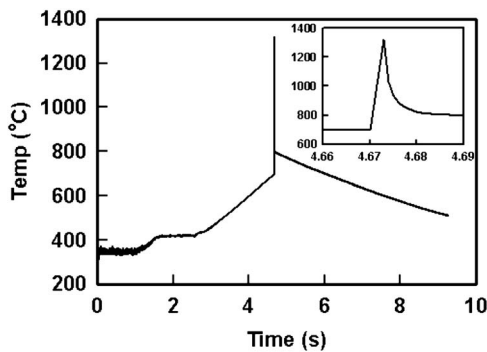


FIG. 2. Annealing program for flash anneal experiment with a peak temperature of 1322 °C. Inset shows temperature trajectory during main flash.

sheet resistance mapping was performed by a KLA Tencor RS100.

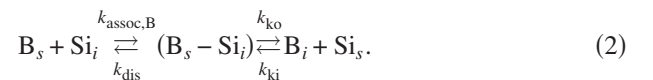
III. MODEL FORMULATION

The boron diffusion model is based on an earlier version⁵ and has been implemented by the profile simulator FLOOPS 2000.¹¹ The model represents boron diffusion within crystalline silicon, with no special provision for preamorphizing implantation. Yet most spike and flash annealing technology employ a brief preheating step before the main temperature ramp. Considerable solid phase epitaxial regrowth of the amorphized layer to reform crystalline Si typically occurs during preheating. Although regrowth does not always proceed to completion and boron diffusion/activation behavior can differ in details from cases when preamorphization is not used,¹² the model may still apply in many respects depending upon the exact processing protocol.

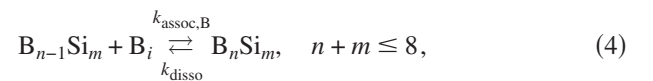
The model utilizes continuum equations to describe the reaction and diffusion of boron interstitial atoms and related defects in silicon. These equations have the general form for species *i*:

$$\frac{\partial C_i}{\partial t} = -\frac{\partial J_i}{\partial x} + G_i, \quad (1)$$

where C_i , J_i , and G_i denote the concentration, flux, and net generation rate of species *i*, respectively. The flux J_i consists of Fickian term and electric drift motion. The net generation G_i incorporates terms associated with cluster formation/dissociation and kick-in/kick-out reactions between interstitials and the lattice through the formation of a boron-interstitial complex,¹³



The reactions for the clustering of interstitials for pure Si and mixed B-Si clusters are



where the index of *m* and *n* denote the number of silicon and boron interstitials in the cluster, respectively. The maximum cluster size was set to eight, with the eight-atom dissociation energy equated to that for very large clusters.¹⁴

The effectiveness of the surface in removing boron and silicon interstitials was quantified by the surface annihilation probabilities,¹⁵ S_B and S_{Si} respectively, which are incorporated in the model boundary condition as

$$-D_k \left. \frac{\partial C_k}{\partial x} \right|_{x=0} = J_{total,k} S_k, \quad \text{where } k = Si_i, B_i. \quad (5)$$

Here, J_{total} denotes the total impinging flux of interstitials. The actual flux at the surface is the product of the total impinging flux and the surface loss probability.

TABLE I. *A priori* model parameters and confidence intervals.

Parameter	Unit	Value	Standard deviation	95% confidence interval half-width	Method	Ref
1. Cluster dissociation–pure Si cluster						
E_2 (size 2)	eV	1.400	0.030	0.060	ML	14
E_3 (size 3)	eV	1.796	a	a	a	a
E_4 (size 4)	eV	2.192	a	a	a	a
E_5 (size 5)	eV	2.588	a	a	a	a
E_6 (size 6)	eV	2.983	a	a	a	a
E_7 (size 7)	eV	3.379	a	a	a	a
$E_8 = E_{\text{large}}$ (large)	eV	3.775	0.003	0.013	MAP	18
2. Cluster dissociation–pure B cluster						
$E_{2,B}$ (size 2)	eV	1.788	0.012	0.024	MAP	17
3. Cluster dissociation–mixed B-Si cluster						
$E_{3,\text{mix}}$ (size 3)	eV	1.750	a	a	a	a
$E_{4,\text{mix}}$ (size 4)	eV	2.100	a	a	a	a
$E_{5,\text{mix}}$ (size 5)	eV	2.450	a	a	a	a
$E_{6,\text{mix}}$ (size 6)	eV	2.800	a	a	a	a
$E_{7,\text{mix}}$ (size 7)	eV	3.150	a	a	a	a
$E_{8,\text{mix}} = E_{\text{large,mix}}$ (large)	eV	3.500	b	b	ML	14
4. Kick-in/kick-out reaction						
E_{ko}	eV	0.408	0.008	0.015	MAP	17
E_{ki}	eV	0.458	0.008	0.015	MAP	17
E_{dis}	eV	0.575	0.002	0.004	MAP	17
5. Interstitial diffusion						
$E_{\text{diff,Si}}$	eV	0.764	0.003	0.012	MAP	18
$E_{\text{diff,B}}$	eV	0.359	0.004	0.008	MAP	17
6. Surface annihilation of interstitials						
S_{Si_i}	-	2.5×10^{-5}	c	c	c	54
S_{B_i}	-	2.5×10^{-5}	c	c	c	54

^aDissociation energies of intermediate clusters were determined by linear interpolations of ML /MAP estimates.

^bML estimation was based on only a single published value.

^cValue of surface annihilation probabilities set based on experimental data in Ref. 19.

Importantly, the present simulations incorporated near-surface band bending⁸ for spike and flash annealing but not for soak annealing because the soak annealing time was much longer than the time required to anneal out the implantation-induced electrically active defects at the native oxide interface.¹⁶ Detailed reasoning can be found in Ref. 5. For spike and flash annealing, band bending was incorporated by setting the surface Fermi level at 0.4 eV above the valance band edge, in accord with the experimental value.¹⁶ That is, the potential Ψ at the surface was represented by the boundary condition

$$\Psi_{x=0} = E_v(T)/q + 0.4 \text{ eV}/q. \quad (6)$$

A priori estimates of the kinetic parameters that govern the diffusion and reaction of boron have been determined previously⁵ by maximum likelihood (ML) estimation^{13,14} and maximum *a posteriori* (MAP) estimation^{17,18} which

optimally combine a variety of experimental and computational data.⁷ Table I summarizes the *a priori* estimates and the associated standard deviations. This *a priori* parameter set has proven capable of accurately simulating profiles for soak and spike annealing,⁵ as Fig. 3(a) shows for examples of spike annealing at 1000 °C and 1050 °C.

However, initial simulations showed that the *a priori* parameters gave poor agreement with experimental profiles for flash annealing. As shown in Fig. 3(b), the model failed to capture the shape of the annealed profile. Moreover, the temperature dependence of profile spreading was poorly reproduced. The simulated profiles for 1256 °C and 1322 °C almost overlap with each other, whereas a significant difference in profile shape is observed experimentally. The discrepancy between experiment and simulation for flash annealing motivated further model refinement in this regime of significantly higher temperatures and shorter times. The refinement utilized parameter sensitivity analysis and MAP estimation.

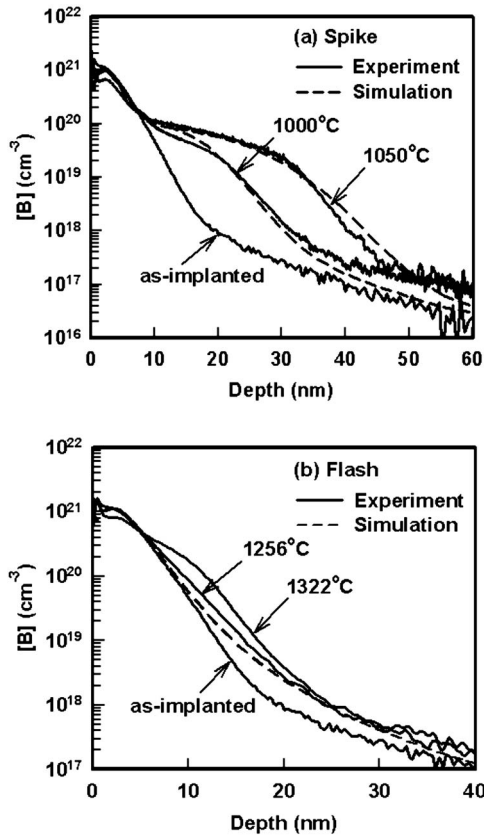


FIG. 3. Experimental and simulated boron profiles using *a priori* parameter estimates for (a) spike annealing to 1000 °C and 1050 °C and (b) flash annealing to 1256 °C and 1322 °C. The flash annealing simulations essentially overlay each other and are indistinguishable from each other, in contrast to the experimental profiles.

IV. METHODS FOR IMPROVED PARAMETER ESTIMATION

A. Parameter sensitivity analysis

Parameter sensitivity analysis quantifies the influence of perturbations in model parameters on the model outputs and has been widely applied in analysis and design of chemical systems.^{20,21} The analysis determines which model parameters need to be estimated or calculated most accurately for the purpose at hand and which parameters can be largely ignored.

Sensitivity analysis has been applied to the activation energies of elementary kinetic steps governing diffusion of implanted isotopic silicon¹⁸ during soak annealing and of boron¹⁴ during spike annealing. The present study of boron is based on a model⁵ that has advanced considerably over that employed in Ref. 14, however, both in sophistication of the physics as well as the domain of relevant temperatures. These changes warranted that the sensitivity analysis be reconstructed, albeit with the focus still upon profile spreading and dopant activation.

Sensitivity analysis requires the formulation of a matrix F of sensitivity coefficients that includes the partial derivatives of the variables β_k with respect to the dependent variables P_j ,²²

$$F_{j,k} = F(P_j; \beta_k) = \frac{\partial P_j(\beta_k)}{\partial \beta_k}, \quad (7)$$

where $F(P_j; \beta_k)$ denotes the sensitivity coefficient of the j th measurement to the k th parameter. Since the numerical values of surface annihilation probability, S , and the various activation energies differ by five orders of magnitude (see Table I), the sensitivities are normalized to allow a more direct comparison of the relative importance of these parameters. The matrix \hat{F} of normalized sensitivity coefficients is defined as,²³

$$\hat{F}_{j,k} = \hat{F}(P_j; \beta_k) = \frac{\partial P_j(\beta_k)}{\partial \ln \beta_k} = \beta_k \frac{\partial P_j(\beta_k)}{\partial \beta_k}. \quad (8)$$

In this work, the sensitivity coefficients were estimated by the finite difference method:

$$\hat{F}(P_j; \beta_k) \approx \beta_k \frac{\Delta P_j}{\Delta \beta_k} = \beta_k \left(\frac{P_j(\beta_k + \Delta \beta_k) - P_j(\beta_k - \Delta \beta_k)}{2\Delta \beta_k} \right). \quad (9)$$

The present analysis was aimed at the sensitivity of model parameters to metrics describing profile spreading and dopant activation. For profile spreading, the total sensitivity for the k th parameter, Φ_k^{Profile} , is given by the sum of squares of the sensitivity coefficients \hat{F} over the entire depth of the boron profile,

$$\Phi_k^{\text{Profile}} = \sum_{p=1}^{N_d} \left(\frac{C_{p,\beta_k+\Delta\beta_k} - C_{p,\beta_k-\Delta\beta_k}}{2\Delta\beta_k/\beta_k} \right)^2, \quad (10)$$

where N_d denotes the total number of data points in the boron profile, and $\Delta\beta_k/\beta_k=0.1$. The parametric sensitivity coefficient for dopant activation Φ_k^{Rs} can be determined similarly,

$$\Phi_k^{\text{Rs}} = \left(\frac{R_{s,\beta_k+\Delta\beta_k} - R_{s,\beta_k-\Delta\beta_k}}{2\Delta\beta_k/\beta_k} \right)^2, \quad (11)$$

The value of sheet resistance R_s is related to the active dopant concentration C_s by²⁴

$$R_s = \frac{1}{q \int_0^{x_j} \mu(x) C_s(x) dx}, \quad (12)$$

where q and μ are the electron charge and the majority charge carrier mobility, respectively. The junction depth x_j is calculated at $[B]=5 \times 10^{18} \text{ cm}^{-3}$.

B. MAP estimation

MAP estimation determines the most likely values of parameters when prior information is available.^{25,26} MAP estimation optimally combines prior statistical information of the parameter estimates with additional experimental data to obtain improved *a posteriori* estimates. For the present case, prior information about the parameters^{13,14,17,18} already exists from ML estimation and MAP estimation based on density functional theory calculations, isolated experiments from the literature, and previous experiments performed in the Uni-

versity of Illinois laboratory on boron and silicon diffusion. Table I shows these *a priori* estimates. Reported experimental data include experimental soak-, spike-, and flash-annealed boron concentration profiles obtained as described above.

Details of the formulation of MAP estimation have been provided in Refs. 17 and 18. In brief, MAP estimation can be equivalently posed as a minimization problem,

$$\min_{\beta} \left\{ (\beta - \mu)^T V_{\mu}^{-1} (\beta - \mu) + \sum_{j=1}^d [Y_j - P_j(\beta)]^T V_{e,j}^{-1} [Y_j - P_j(\beta)] \right\}, \quad (13)$$

where β denotes the vector of estimated parameters, μ the vector of corresponding *a priori* parameter estimates, V_{μ} the prior parameter covariance matrix, d the total number of anneal experiments, Y_j the vector of experimental observations, and P_j the vector of model predictions. The measurement covariance matrix for the j th experimental data, $V_{e,j}$, was estimated previously¹⁵ by the measurement of n different SIMS profiles on the same specimen.

For computational efficiency, the elements within β are chosen to exclude activation energies to which the model has little sensitivity (based on the results of sensitivity analysis). A hyperellipsoidal confidence region quantifies the uncertainty in the estimates via the relation

$$E_{\beta} = \{ \beta : (\beta - \beta_{\text{true}})^T V_{\beta^*}^{-1} (\beta - \beta_{\text{true}}) \leq \chi_{\alpha}^2(p) \}, \quad (14)$$

where α denotes the confidence level, χ denotes the chi-squared distribution with p degrees of freedom, and V_{β^*} is the covariance of $(\beta^* - \beta_{\text{true}})$ estimated by

$$\text{cov}(\beta^* - \beta_{\text{true}}) = V_{\beta^*} \approx \left(F^T \begin{pmatrix} V_{e,1} & 0 & 0 \\ 0 & \ddots & 0 \\ 0 & 0 & V_{e,d} \end{pmatrix}^{-1} F + \begin{pmatrix} V_{\mu}^{-1} & 0 \\ 0 & 0 \end{pmatrix} \right)^{-1}, \quad (15)$$

where β^* and β_{true} denote the best estimate and the true value of the vector of parameters, respectively, and each 0 is a matrix of zeros of compatible dimensions. The matrix F is the sensitivity matrix of the vector of model predictions,

$$P = [P_1, \dots, P_d]^T \quad (16)$$

with respect to the vector of parameters β , computed from Eq. (7). The hyperellipsoidal confidence region can be visualized by approximate confidence intervals:²⁷

$$\beta_k^* - \sqrt{\chi_{\alpha}^2(p) V_{\beta^*,kk}} \leq \beta_{\text{true},k} \leq \beta_k^* + \sqrt{\chi_{\alpha}^2(p) V_{\beta^*,kk}} \quad (17)$$

V. RESULTS AND DISCUSSION

A. Parameter sensitivity analysis

Table II shows values of the sensitivity coefficients for profile spreading and sheet resistance for soak, spike, and

flash annealing. Comparisons among coefficients can be made validly only for coefficients within a given group (i.e., in the same column). The absolute magnitudes of the coefficients may be useful for some purposes, but this work concerns itself with the relative magnitudes. The results for spike annealing agree qualitatively with a previous sensitivity analysis for spike annealing that employed an earlier and more primitive version of the model.¹⁴ The most influential activation energies are those for interstitial boron diffusion, dissociation of large clusters, dopant kick-in reaction, and dissociation of the (B-Si) complex to liberate either interstitial B (kick-out) or Si.

The coefficients in Table II show that the major difference in the sensitivity results among the three annealing regimes lies in the increased relative importance of the dissociation energies for the B-Si mixed clusters as time scale increases (and maximum temperature decreases), particularly for the largest mixed cluster, $E_{\text{large,mix}}$. The sensitivity coefficient for this parameter is more than one order of magnitude higher than that for boron diffusion and kick-in/kick-out reactions in soak annealing but is one order of magnitude lower in flash annealing.

The sensitivity of the dissociation energy of the second largest Si-B cluster, $E_{7,\text{mix}}$, is higher than that of $E_{\text{large,mix}}$ for flash annealing, but the opposite trend is observed for soak and spike annealing. This decreased importance of $E_{\text{large,mix}}$ can be explained by retarded dissociation of large clusters when the time scale decreases (or equivalently, when the ramp rate increases). It has been shown previously²⁸ that at a given temperature T , the dissociation energy E^* of the most actively dissociating clusters depends upon the ramp rate ϕ according to

$$\left(E^*/kT - \frac{1}{2} \right) \exp \left(E^*/kT - \frac{1}{2} \right) = A_{\text{disso}} T / \phi, \quad (18)$$

where A_{disso} is the pre-exponential factor for cluster dissociation. For flash annealing, substituting $T=1595$ K (1322 °C, a typical maximum in flash processing) and the experimental ramp-up rate of $\phi=2 \times 10^5$ °C/s gives $E^*=3.02$ eV, which is within 10% [i.e., $\Delta\beta/\beta$ in Eq. (10)] of $E_{7,\text{mix}}$ (3.15 eV). Therefore, the next-to-largest clusters are dissociating, but the largest clusters ($E_{\text{large,mix}}=3.5$ eV) have not yet dissociated at the peak temperature for flash annealing. For spike annealing, substituting $T=1323$ K (1050 °C, a typical maximum in spike processing) and the experimental ramp-up rate of $\phi=168$ °C/s gives $E^*=3.27$ eV, which is above $E_{7,\text{mix}}$ and within 10% of $E_{\text{large,mix}}$. Thus, the next-to-largest clusters have already largely dissociated, and the largest clusters dominate most dissociation activity. For the case of soak annealing, the dissociation state of the largest clusters can be estimated by calculation of the constant-temperature time constant. At 900 °C, the time constant for the dissociation of the largest clusters equals $(k_{\text{disso}})^{-1} = [A_{\text{disso}} \exp(-3.5/kT)]^{-1} = 185$ s. For an annealing time of 1 h, the largest clusters are the last ones to dissociate and dominate the final state of the profile.

This calculation can explain two aspects of the results of the sensitivity analysis. Since the largest clusters have not yet dissociated for the case of flash annealing, the corresponding

TABLE II. Sensitivity coefficients for profile spreading and sheet resistance.

Parameter	Profile sensitivity $\Phi^{\text{Profile}} (\text{cm}^{-3})^2$			Resistance sensitivity $\Phi^{\text{Rs}} (\Omega/\text{sq})^2$		
	Soak	Spike	Flash	Soak	Spike	Flash
1. Cluster dissociation–pure Si clusters						
E_2	1.1×10^{35}	1.2×10^{39}	8.9×10^{38}	7.8×10	1.6×10	1.4×10^{-3}
E_3	1.9×10^{38}	3.5×10^{40}	7.9×10^{40}	1.3×10^2	1.3×10	1.6
E_4	3.7×10^{37}	2.3×10^{39}	2.4×10^{39}	1.4×10^3	3.8×10^2	2.5×10^{-1}
E_5	1.3×10^{38}	7.7×10^{39}	8.0×10^{40}	3.4×10^3	2.0×10^3	8.7×10^{-1}
E_6	4.7×10^{37}	3.1×10^{40}	2.8×10^{41}	5.4×10^2	3.9×10^2	3.5×10^{-1}
E_7	4.1×10^{35}	3.8×10^{37}	1.3×10^{39}	6.0×10^{-1}	1.7×10^{-1}	1.1×10^{-3}
E_{large}	7.6×10^{35}	4.6×10^{38}	1.6×10^{38}	3.6×10^{-1}	7.1×10^{-4}	5.6×10^{-5}
2. Cluster dissociation–pure B clusters						
$E_{2,B}$	1.8×10^{38}	4.0×10^{42}	7.1×10^{42}	2.6×10^4	7.4×10^3	8.8×10^{-2}
3. Cluster dissociation–mixed B-Si clusters						
$E_{3,\text{mix}}$	4.1×10^{38}	1.7×10^{42}	1.1×10^{42}	1.2×10^4	1.1×10^3	1.1
$E_{4,\text{mix}}$	3.1×10^{37}	6.3×10^{39}	3.6×10^{41}	4.8×10^3	8.8×10^2	1.5×10^{-1}
$E_{5,\text{mix}}$	1.4×10^{40}	4.0×10^{41}	1.8×10^{42}	6.8×10^3	8.5×10^2	1.5×10
$E_{6,\text{mix}}$	2.5×10^{42}	9.2×10^{42}	4.9×10^{42}	1.2×10^4	2.0×10^4	2.3×10^3
$E_{7,\text{mix}}$	1.2×10^{43}	3.3×10^{43}	9.7×10^{42}	1.8×10^4	1.0×10^5	1.2×10^4
$E_{\text{large,mix}}$	4.4×10^{43}	1.0×10^{44}	1.0×10^{42}	6.6×10^4	2.9×10^6	4.3×10^5
4. Kick-in/kick-out reaction						
E_{ko}	7.8×10^{41}	1.2×10^{44}	9.7×10^{43}	1.6×10^6	8.9×10^5	3.6×10^2
E_{ki}	9.9×10^{41}	1.5×10^{44}	1.2×10^{44}	2.0×10^6	1.1×10^6	4.8×10^2
E_{dis}	1.6×10^{42}	3.9×10^{43}	4.3×10^{43}	2.0×10^6	1.2×10^6	4.3×10^2
5. Interstitial diffusion						
$E_{\text{diff,Si}}$	2.8×10^{34}	3.8×10^{38}	2.9×10^{40}	9.1	7.9	1.3×10^{-5}
$E_{\text{diff,B}}$	6.2×10^{41}	1.4×10^{43}	9.5×10^{42}	8.1×10^5	4.8×10^5	1.5×10^2
6. Surface annihilation of interstitials						
S_{Si_i}	6.5×10^{39}	1.2×10^{40}	6.2×10^{37}	5.59×10^{-3}	2.20×10	3.1
S_{B_i}	1.1×10^{38}	1.7×10^{39}	9.7×10^{37}	3.53×10^{-1}	1.14×10	8.1

sensitivity coefficient of its dissociation energy is less than that of the next-largest cluster ($E_{7,\text{mix}}=3.15$ eV), which is actively dissociating at the top of the flash. The opposite trend is observed for soak and spike annealing, for which the largest clusters dominate dissociation activity.

In addition, some of the interstitials liberated at the top of the flash can accrete onto the remaining next-largest clusters to form the largest size, as shown in Eqs. (3) and (4). However, no equivalent interstitial sink exists in the simulation if the largest cluster is also dissociating, as in the case of spike and soak anneals. If the largest clusters are dissociating, the effect on interstitial release will be more pronounced than that of dissociation of intermediate clusters. This effect explains the decreased relative importance of cluster energetics compared to kick-in/kick-out reactions as ramp rate increases. In soak annealing, $E_{\text{large,mix}}$ has the highest sensitivity among all model parameters. In spike annealing, the dissociation of an intermediate size cluster (i.e., $E_{7,\text{mix}}$) has a sensitivity coefficient similarly large to those of the activation energies for kick-in/kick-out reactions. And in flash annealing, the dissociation of an intermediate size cluster (i.e., $E_{7,\text{mix}}$) has lower sensitivity than the activation energies of kick-in/kick-out reactions.

In contrast to previous work,¹⁴ the present work examined the influences of pure Si clusters and mixed B-Si clusters separately. Table II shows that energetics of dissociation of pure Si and mixed B-Si clusters have different sensitivity coefficients, with the dissociation energies of mixed B-Si clusters exerting more influence than those of pure Si clusters. This observation validates the suggestion made in a previous silicon self-diffusion study¹⁸ that the standard deviation for pure Si cluster energetics is underestimated by setting sensitivities equal for pure Si and mixed B-Si clusters.

The total sensitivities for the surface annihilation probability S are low compared to the clustering and kick-in/kick-out energetics. However, note that the present sensitivity analysis quantifies the change in boron profile upon a perturbation of only 10% in the model parameter. Although the sensitivity coefficient for the surface annihilation probability is rather small for the specific value chosen here, that situation could change under other circumstances. In contrast to activation energies in the model, the surface annihilation probability can vary (sometimes controllably) by several orders of magnitude depending on surface conditions.^{7,18} Hence, it would be incorrect to conclude based upon the

TABLE III. Refined MAP estimates and confidence intervals.

Parameter	MAP estimate	Standard deviation	95% confidence interval half-width
$E_{6,mix}$	2.729	0.008	0.034
$E_{7,mix}$	2.960	0.003	0.014
$E_{large,mix}$	3.697	0.003	0.011
E_{ko}	0.411	0.002	0.007
E_{ki}	0.464	0.002	0.007
E_{dis}	0.574	0.001	0.005
S_{soak}	5.180×10^{-5}	2.296×10^{-6}	8.612×10^{-6}
S_{spike}	4.476×10^{-5}	2.417×10^{-6}	9.065×10^{-6}
S_{flash}	7.915×10^{-5}	3.690×10^{-6}	1.384×10^{-5}

sensitivities in Table II that surface interstitial annihilation cannot exert strong effects on boron diffusion and activation.

For the three annealing regimes studied, parameters that matter most in profile spreading are also important in dopant activation. This suggests that dopant diffusion and activation are highly correlated, which is consistent with the well-known trade-off relation observed experimentally between junction depth and sheet resistance.²⁹

B. MAP estimation

Based on the results of parameter sensitivity analysis, the vector of parameters for MAP estimation was formulated to include the four most influential parameters from each of the soak, spike, and flash annealing protocols. The vector was also set to include the corresponding surface loss probabilities,

$$\beta^T = [E_{6,mix}, E_{7,mix}, E_{large,mix}, E_{ko}, E_{ki}, E_{dis}, S_{soak}, S_{spike}, S_{flash}]. \quad (19)$$

Even though the sensitivity coefficients for S are rather low under present conditions, the database for values of S is very small. The present analysis is capable of adding to that database. The soak annealing experiments employed a different surface treatment from the spike and flash experiments, and S can vary significantly with even small changes in the chemical state of the surface.⁷ S is also believed to vary (rather weakly) with temperature on Si(100).³⁰ As the maximum temperatures vary by more than 400 °C in these experiments, changes in S may occur. The present work assumes equal surface loss probabilities for boron and silicon interstitials, $S_{B_i} = S_{Si_i}$. The annihilation probabilities could in principle differ for Si and B. However, as of yet there is insufficient scientific understanding to predict the magnitude of such a difference, and the present model sought to minimize the number of independently variable parameters.

Table III shows the MAP estimates of the model parameters and the associated 95% confidence intervals. Figure 4 shows examples of experimental and simulated profiles using the refined estimates. Values of sheet resistance are also included. There is significant improvement in profile fit after MAP estimation for the flash annealed profile, with the good agreement in soak and spike annealing utilizing *a priori* estimates retained.

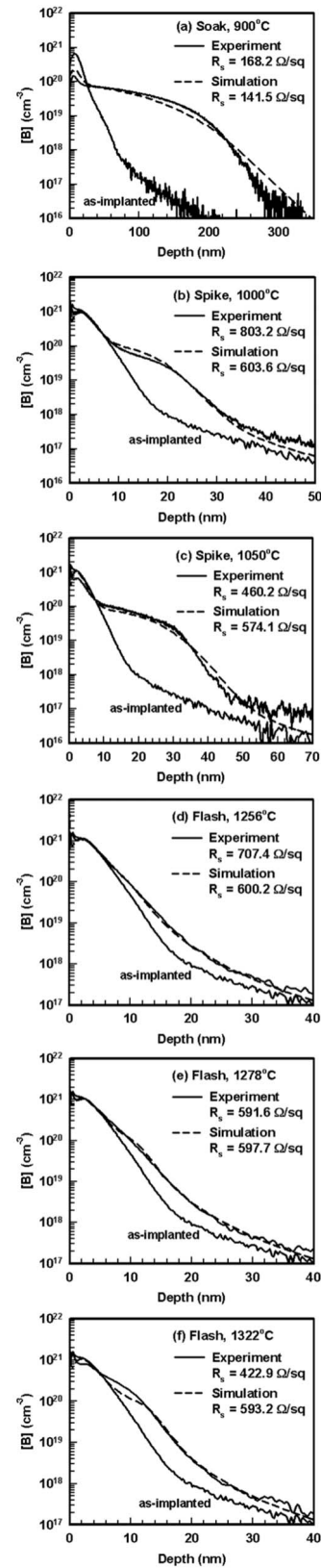


FIG. 4. Experimental and simulated boron profiles with refined MAP parameter estimates for (a) soak annealing at 900 °C, (b) spike annealing at 1000 °C, (c) spike annealing at 1050 °C, (d) flash annealing at 1256 °C, (e) flash annealing at 1278 °C, and (f) flash annealing at 1322 °C. Fits are good over the entire range of conditions.

Figure 5 shows the trade-off relation between sheet resistance and junction depth for both spike and flash annealing. Figure 5 also shows corresponding experimental data

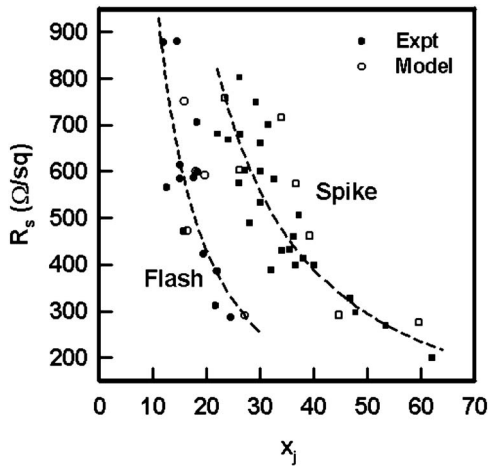


FIG. 5. Relation between sheet resistance and junction depth (at $[B]=5 \times 10^{18} \text{ cm}^{-3}$) for spike and flash anneals. Experimental data for spike annealing (Refs. 29 and 31–38) include results for implanted B and BF_2 annealed with peak temperatures of 1000–1050 °C (implant conditions: B: 0.2–2 keV, 5×10^{14} – $2 \times 10^{15} \text{ cm}^{-2}$; BF_2 : 1.1–2.2 keV, $1 \times 10^{15} \text{ cm}^{-2}$, without preamorphization). Experimental data for flash annealing (Refs. 39 and 40) include results from experiments utilizing similar implant conditions with peak temperatures of 1256–1350 °C. Initial conditions for simulations employ experimental as-implanted profiles (B, 0.5–3 keV, 1×10^{15} – $2 \times 10^{15} \text{ cm}^{-2}$, without preamorphization) as well as simulated implanted profiles from the Dual Pearson model (Ref. 41) (BF_2 , 1 keV, 5×10^{14} – $1 \times 10^{15} \text{ cm}^{-2}$, without PAI). Dashed lines are guides for the eyes. Simulations track experimental trends quite well.

from spike^{29,31–38} and flash^{39,40} annealing that have been extracted from the literature. The model output agrees well with the experimental trend for both annealing schemes and confirms the simultaneous improvement in dopant activation and junction depth characteristic of flash annealing.

All of the experimental MAP parameter estimates lie within the *a priori* confidence intervals shown in Table I. Thus, these MAP estimates lie within the expected distances of the prior estimates but have substantially smaller standard deviations. Since the various model parameters exert different sensitivities in different annealing methods, incorporation of the broader range of experimental data having widely divergent time scales and peak temperatures served to impose tight constraints on the values of parameters and thereby improve the accuracy of the estimates.

The value of S for flash annealing is about a factor of 1.5 higher than that for soak and spike annealing. The difference may originate from differences in surface conditions (even subtle) due to processing protocols and possibly in processing temperature. However, the values of S for all three methods are much smaller than the maximum value of ~ 0.05 (Ref. 6) measured for an atomically clean, chemically active Si(100) surface. The small values in the present experiments probably arise from oxygen in the processing environment.

C. Effects of annealing protocol on boron diffusion

The model and parameter set have demonstrated their capability to simulate key aspects of boron diffusion and activation over a maximum temperature range greater than 400 degrees wide (from 900 °C to 1322 °C) and more than

six orders of magnitude in time scales (from ~ 1 ms to 1 h). Such a broad range of applicability offers confidence that the model reproduces interstitial concentrations accurately enough to serve as the input for an analytical description of the primary mechanisms governing boron diffusion and activation during the transient heating characteristic of spike and millisecond annealing.

An analytical expression to rationalize the effects of ramp rate on boron profile spreading near the junction during spike annealing has been developed previously.^{28,42} The expression was based on the simple random-walk diffusion equation $X_{\text{lattice}}^2 = 6Dt$, with X_{lattice} being the mean square displacement of diffusing dopant interstitials that sometimes exchange with the lattice, and t being a characteristic diffusion time. The following expression was derived for X_{lattice} :

$$X_{\text{lattice}}^2 = 6\lambda^2 k_{\text{assoc}} [\text{Si}_i] t_{\text{max}} \times \exp[(E_{\text{ki}} - E_{\text{diff},B_i})/kT](1-b)/b, \quad (20)$$

where λ denotes the site-to-site interstitial hop length of 0.27 nm. The reaction constant k_{assoc} equals $4\pi a D_{\text{Si}}$, wherein a and D_{Si} denote the capture radius and the diffusivity of silicon interstitials, respectively. The time t_{max} represents a characteristic time span over which the wafer remains near the peak temperature (within 95% of the peak), and $[\text{Si}_i]$ denotes the concentration of Si interstitials at the peak temperature, which is given by the simulation model. The variable b represents the branching ratio between the dissociation reaction of the B_s – Si_i complex to form either B_i or Si_i . Assuming that the rate constants for these two reactions share the value for the same pre-exponential factor A , the branching ratio can be expressed as

$$b = \frac{A \exp(-E_{\text{dis}}/kT)}{A \exp(-E_{\text{dis}}/kT) + A \exp(-E_{\text{ko}}/kT)} = \frac{1}{1 + \exp\left(\frac{E_{\text{dis}} - E_{\text{ko}}}{kT}\right)}. \quad (21)$$

With the *a priori* parameter set from Ref. 17, Eq. (20) showed²⁸ good agreement (within 10%–20%) with experimental spreading profiles for spike annealing over the relatively limited range of conditions examined. With the present refined MAP parameter estimates, Eq. (20) should yield good agreement with the experimental spreading observed over a much broader temperature range. Indeed, Eq. (20) estimates profile spreading (at $[B]=5 \times 10^{18} \text{ cm}^{-3}$) of 20.6 nm and 4.8 nm for spike (1050 °C) and flash (1322 °C) annealing, respectively. These analytical estimates agree exceptionally well with the experimental observations of 21.6 nm and 4.7 nm.

The relatively simple form of Eq. (20) permits clear insights into the differing effects of spike and millisecond annealing on boron diffusion. Table IV shows key quantities composing Eq. (20) calculated for the particular experimental conditions described in this work but also representative of conditions typically employed in these annealing protocols. The major difference between the two methods lies in the values of $k_{\text{assoc}}[\text{Si}_i]$ and t_{max} . As discussed in Ref. 28,

TABLE IV. Key quantities in Eq. (20) for typical conditions in spike and flash annealing.

Parameter	Unit	Spike anneal (1050 °C)	Flash anneal (1322 °C)
t_{\max}	s	6.3×10^{-1}	6.3×10^{-4}
$k_{\text{assoc}}[\text{Si}_i]$	s	1.4×10^2	1.2×10^4
$t_{\max} \times k_{\text{assoc}}[\text{Si}_i]$	-	88	7.6
$(1-b)/b$	-	4.2	3.3
$\exp((E_{\text{ki}} - E_{\text{diff,B}})/kT)$	-	2.5	2.2
X (model)	nm	20.6	4.8
X (expt.)	nm	21.6	4.7

$(k_{\text{assoc}}[\text{Si}_i])^{-1}$ represents a characteristic time for the kick-out of substitutional boron from the lattice by Si interstitials, thereby rendering the boron mobile. The combined quantity $t_{\max} \times k_{\text{assoc}}[\text{Si}_i]$ represents the number of liberation events near the temperature peak, where most dopant diffusion occurs. Although $k_{\text{assoc}}[\text{Si}_i]$ is almost two orders of magnitude larger for flash annealing than for spike annealing—owing mainly to the higher interstitial concentration—the corresponding time scale t_{\max} is almost three orders of magnitude smaller. As a result of this compensation, flash annealing reduces the profile spreading significantly.

This explanation differs from that invoked to explain the benefits of increased ramp rate in spike annealing.⁴² In that case, a similar analysis showed that fast ramp rates (on the order of 400 °C/s) to a fixed peak temperature reduce the time during which the implanted profile is exposed to the maximum concentrations of Si interstitials. The fast ramp also pushes the dissociation of large interstitial clusters (with high dissociation energies) up to higher temperatures. For a constant peak temperature, this dissociation “delay” during the ramp slightly reduces the maximum concentrations of Si interstitials. Both the shortened exposure time and reduced interstitial concentration inhibit dopant diffusion. In the millisecond annealing, however, the peak temperature greatly exceeds that for spike annealing. Thus, even though the faster ramping of millisecond annealing pushes up the cluster dissociation temperatures, the maximum Si interstitial concentrations still greatly exceed those for spike annealing. The benefits from millisecond annealing derive from the shortened time scale that outweighs the effects of increased Si interstitial concentration.

This physical picture points to even further potential reductions in junction depth through methods that operate on even shorter time scales than flash annealing, such as annealing with scanned continuous-wave^{43,44} or pulsed^{45,46} lasers. However, the effects of very fast methods on dopant activation complicate matters, as discussed further below.

D. Effects of annealing protocol on boron activation

Equation (20) also helps to explain the improved dopant activation seen in millisecond annealing, although the analysis must be applied in a spatially dependent way. When clusters dissociate to release boron interstitial atoms, those interstitials diffuse until sequestered either by kick-in to the

lattice [Eq. (2)] or by reaccrion back into remaining clusters [Eq. (4)]. Sequestration by the lattice leads to electrically active boron that remains largely immobile but electrically active until a Si interstitial arrives to drive a kick-out reaction. Equation (20) gives the typical distance that a typical boron atom released from a cluster will move during the annealing cycle if this sequestration mechanism dominates. Because $[\text{Si}_i]$ varies with depth into the wafer due to varying concentrations of clusters, X_{lattice} also varies with depth. Figure 6 shows this variation in X_{lattice} calculated via Eq. (20) for typical maximum temperatures in spike and flash annealing. In these calculations, the values of $[\text{Si}_i]$ originated from simulations. In all cases, the spatial variation of X_{lattice} exhibits a maximum value near the peak of the interstitial cluster concentration at depths < 5 nm and drops off to lower values in directions toward the interstitial sink regions both at the surface and in the bulk. The maximum simply reflects the increased rate of Si interstitial creation where many clusters are dissociating. For similar reasons, X_{lattice} at any depth increases as the maximum temperature rises and induces more clusters to dissociate.

Figure 6 also shows diffusion distances X_{cluster} calculated with the alternative assumption that sequestration of B interstitials into remaining clusters dominates. Typically only the largest clusters (that have the highest dissociation energies) still exist intact at the highest annealing temperatures. Thus, the B diffusion distances limited by cluster sequestration can be estimated as simply the average spacing between the largest clusters (size 8) in the model:

$$X_{\text{cluster}} = [\text{largest clusters}]^{-1/3}. \quad (22)$$

The values of X_{cluster} also vary with depth but in a direction generally opposite to X_{lattice} because X_{lattice} increases with cluster concentration while X_{cluster} decreases.

Figure 7 plots the same results as Fig. 6 but in a way that facilitates direct comparison of various annealing protocols regarding the behavior of X_{cluster} and X_{lattice} . Figure 7 shows that X_{cluster} remains largely invariant with annealing conditions, while X_{lattice} varies strongly. The X_{lattice} curves for spike annealing lie substantially above those for flash annealing.

This difference among annealing protocols for X_{lattice} lies at the heart of the improved electrical activation performance of flash annealing compared to spike for the following reason. The dominant B sequestration mode is simply the mechanism that has the smallest value of X . A superposition of the X_{cluster} and X_{lattice} curves indicates which mechanism dominates as a function of depth. Figure 8 shows schematically such superposition for spike and flash annealing. For the typical conditions examined here, cluster sequestration dominates from the surface to a depth x_{cross} , while lattice sequestration dominates deeper within the solid. The crossover point is typically shallower than the junction by 5–10 nm. The strong variation in the X_{lattice} curves with annealing conditions means that the position of x_{cross} is considerably deeper for spike than for flash annealing. In consequence, a

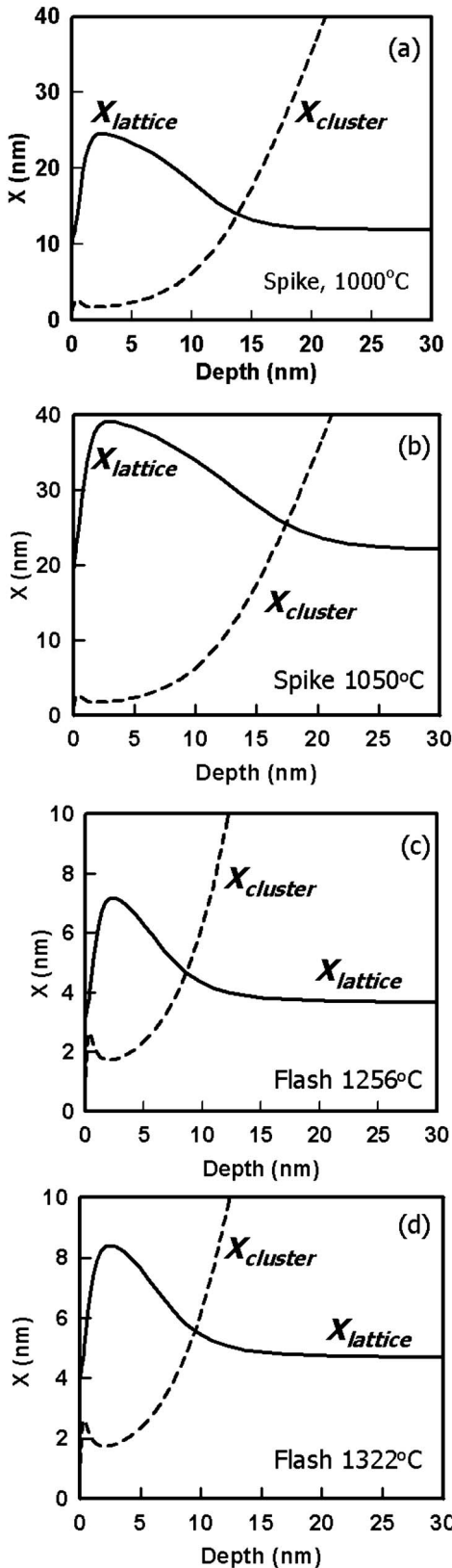


FIG. 6. Variation in average diffusion distances X of boron interstitial atoms before sequestration by lattice and cluster mechanisms, calculated via Eqs. (20) and (22) for typical maximum temperatures in spike and flash annealing. $X_{lattice}$ and $X_{cluster}$ vary with depth because of variations in local cluster concentrations.

smaller total fraction (integrated over the profile) of boron released from clusters winds up in electrically active lattice sites for spike than for flash annealing.

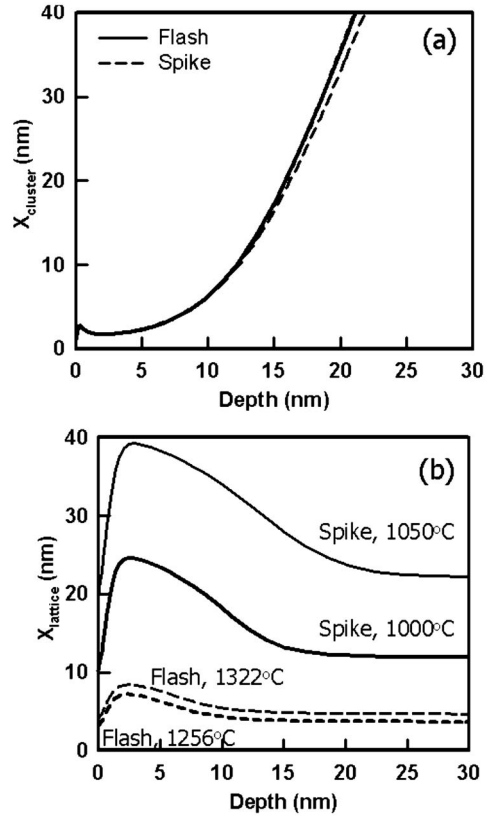


FIG. 7. Data of Fig. 6 replotted to separately compare $X_{lattice}$ and $X_{cluster}$ for spike and flash annealing. $X_{cluster}$ shows little variation, but $X_{lattice}$ changes a great deal.

E. Implications for microsecond annealing

An important limit exists to the benefits of continuing to decrease the annealing time. The temperature of incipient wafer damage sets this limit. Equation (18) indicates that, to reach a given degree of cluster dissociation to liberate boron (as embodied in E^*), the maximum annealing temperature must rise as the annealing technique becomes faster (with a faster ramp rate ϕ). Consider the example of pulsed laser

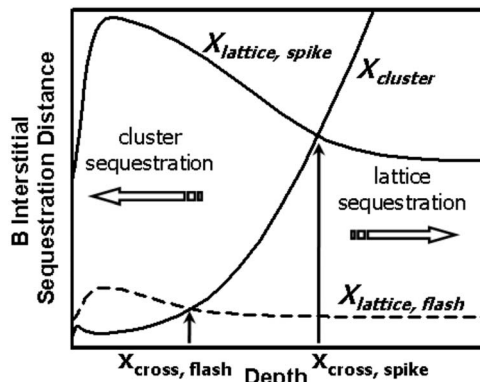


FIG. 8. Superposition of the $X_{cluster}$ and $X_{lattice}$ curves for typical spike and flash annealing conditions. Cluster sequestration dominates from the surface to a depth x_{cross} , while lattice sequestration dominates deeper within the solid. The crossover point is typically shallower than the junction by 5–10 nm. The strong variation of the $X_{lattice}$ curves moves x_{cross} considerably deeper for spike than flash annealing, so a smaller total fraction (integrated over the profile) of boron released from clusters winds up in electrically active lattice sites for spike than for flash annealing.

annealing with a 200 ns pulse⁴⁶ as compared to flash annealing to 1322 °C. In flash annealing, the ramp rate is $\phi=2 \times 10^5$ °C/s, compared to $\phi=3 \times 10^9$ °C/s for the pulsed laser. For this particular flash annealing case, Eq. (18) yields $E^*=3.02$ eV. For the pulsed laser process to reach the same value of E^* (and therefore degree of initial boron release from clusters), the maximum temperature would have to increase vastly up to 2450 °C. This temperature is far above the Si melting point of 1410 °C. The limited cluster dissociation leads to poor dopant activation^{47–49} and, by related mechanisms, to the incomplete removal of EOR defects^{49–51} commonly observed in microsecond annealing.

VI. CONCLUSION

On an empirical basis, multiple continuous-wave laser beam scans⁵¹ or multiple pulses^{45,46} are sometimes employed to mitigate problems with short-time annealing techniques. An alternative approach involves using two-step annealing protocols comprising laser irradiation in conjunction with furnace annealing³ or conventional RTP.^{52,53} The lower ramp-rate step dissociates clusters to improve activation whereas the use of intermediate temperature ensures limited profile spreading. Design of alternatives through laser pulse duration,⁵⁴ number of laser pulses, and varying combinations of laser with furnace annealing steps or RTP can be effected to a reasonable approximation by the sort of mathematical analysis given above.

ACKNOWLEDGMENTS

This work was partially supported by ACS Petroleum Research Fund (Grant No. 43651-AC5) and NSF (Grant No. DMR 07-04354). SIMS for the soak-annealed material was performed at the Center for Microanalysis of Materials, University of Illinois, which is partially supported by the U.S. Department of Energy under Grant No. DEFG02-96-ER45439. We thank Chris Hatem of Varian Semiconductor Equipment Associates for providing the boron-implanted wafer used for soak annealing.

¹See The International Technology Roadmap for Semiconductors, 2006 Update (<http://www.itrs.net/Links/2006update/2006UpdateFinal.htm>).

²T. Gebel, M. Voelskow, W. Skorupa, G. Mannino, V. Privitera, F. Priolo, E. Napolitani, and A. Carnera, *Nucl. Instrum. Methods Phys. Res. B* **186**, 287 (2002).

³S. Baek, S. Heo, H. Choi, and H. Hwang, *J. Vac. Sci. Technol. B* **23**, 257 (2005).

⁴W. Lerch, S. Paul, J. Niess, S. McCoy, T. Selinger, J. Gelpey, F. Cristiano, F. Severac, M. Gavelle, S. Boninelli, P. Pichler, and D. Bolze, *Mater. Sci. Eng., B* **124–125**, 24 (2005).

⁵C. T. M. Kwok, R. D. Braatz, S. Paul, W. Lerch, and E. G. Seebauer, *AICHE J.* (submitted).

⁶C. T. M. Kwok, K. Dev, R. D. Braatz, and E. G. Seebauer, *J. Appl. Phys.* **98**, 013524 (2005).

⁷E. G. Seebauer, K. Dev, M. Y. L. Jung, R. Vaidyanathan, C. T. M. Kwok, J. W. Ager, E. E. Haller, and R. D. Braatz, *Phys. Rev. Lett.* **97**, 055503 (2006).

⁸M. Y. L. Jung, R. Gunawan, R. D. Braatz, and E. G. Seebauer, *J. Appl. Phys.* **95**, 1134 (2004).

⁹M. A. Mendicino and E. G. Seebauer, *Surf. Sci.* **277**, 89 (1992).

¹⁰M. A. Mendicino and E. G. Seebauer, *J. Electrochem. Soc.* **140**, 1786 (1993).

¹¹See Mark Law, University of Florida at Gainesville, <http://www.swamp.tec.ufl.edu/>

¹²S. H. Jain, P. B. Griffin, J. D. Plummer, S. McCoy, J. Gelpey, T. Selinger, and D. F. Downey, *IEEE Trans. Electron Devices* **52**, 1610 (2005).

¹³M. Y. L. Jung, R. Gunawan, R. D. Braatz, and E. G. Seebauer, *AICHE J.* **50**, 3248 (2004).

¹⁴R. Gunawan, M. Y. L. Jung, R. D. Braatz, and E. G. Seebauer, *J. Electrochem. Soc.* **150**, G758 (2003).

¹⁵C. T. M. Kwok, K. Dev, R. D. Braatz, and E. G. Seebauer, *J. Appl. Phys.* **98**, 013524 (2005).

¹⁶K. Dev, M. Y. L. Jung, R. Gunawan, R. D. Braatz, and E. G. Seebauer, *Phys. Rev. B* **68**, 195311 (2003).

¹⁷R. Gunawan, M. Y. L. Jung, E. G. Seebauer, and R. D. Braatz, *AICHE J.* **49**, 2114 (2003).

¹⁸C. T. M. Kwok, K. Dev, R. D. Braatz, and E. G. Seebauer, *Automatica* **44**, 2241 (2008).

¹⁹K. Dev, C. T. M. Kwok, R. Vaidyanathan, R. D. Braatz, and E. G. Seebauer, Proceedings of the 16th International Conference on Ion Implantation Technology, 2006, Vol. 866, p. 50.

²⁰J. R. Leis, S. A. Gallagher, and M. A. Kramer, *Comput. Chem. Eng.* **11**, 409 (1987).

²¹F. D. Van Voorhees and A. Terry Bahill, Proceedings of the IEEE International Conference of Systems, Man and Cybernetics, 1995, Vol. 2, p. 971.

²²R. Tomović and M. Vukobratović, *General Sensitivity Theory* (Elsevier, New York, 1972).

²³E. Rusli, F. Xue, T. O. Drews, P. M. Vereecken, P. Andricacos, H. Deligianni, R. D. Braatz, and R. C. Alkire, *J. Electrochem. Soc.* **154**, D584 (2007).

²⁴F. Cristiano, N. Cherkashin, P. Calvo, Y. Lamrani, X. Hebras, A. Claverie, W. Lerch, and S. Paul, *Mater. Sci. Eng., B* **114–115**, 174 (2004).

²⁵J. V. Beck and K. J. Arnold, *Parameter Estimation in Engineering and Science* (Wiley, New York, 1977).

²⁶G. Sparacino, C. Tombolato, and C. Cobelli, *IEEE Trans. Biomed. Eng.* **47**, 801 (2000).

²⁷H. B. Matthews III, Ph.D. thesis, University of Wisconsin, Madison, 1997.

²⁸M. Y. L. Jung, R. Gunawan, R. D. Braatz, and E. G. Seebauer, *J. Electrochem. Soc.* **151**, G1 (2004).

²⁹A. J. Murrell, E. J. H. Collart, M. A. Foad, and D. Jennings, *J. Vac. Sci. Technol. B* **18**, 462 (2000).

³⁰X. Zhang, M. Yu, C. T. M. Kwok, R. Vaidyanathan, R. D. Braatz, and E. G. Seebauer, *Phys. Rev. B* **74**, 235301 (2006).

³¹D. F. Downey, S. W. Falk, A. F. Bertuch, and S. D. Marcus, *J. Electron. Mater.* **28**, 1340 (1999).

³²A. Mokhberi, P. B. Griffin, J. D. Plummer, E. Paton, S. McCoy, and K. Elliott, *IEEE Trans. Electron Devices* **49**, 1183 (2002).

³³B. Bayha, S. Paul, W. Lerch, D. F. Downey, E. A. Arevalo, X. Hebras, and N. Cherkashin, Proceedings of the 14th International Conference on Ion Implantation Technology, 2002, p. 618.

³⁴B. Bayha, D. Loeffelmacher, W. Lerch, D. F. Downey, and E. A. Arevalo, Proceedings of the 13th International Conference on Ion Implantation Technology, 2000, p. 623.

³⁵S. C. Jain, W. Schoenmaker, R. Lindsay, P. A. Stolk, S. Decocutere, M. Willander, and H. E. Maes, *J. Appl. Phys.* **91**, 8919 (2002).

³⁶A. Agarwal, H.-J. Grossmann, and A. T. Fiory, *J. Electron. Mater.* **28**, 1333 (1999).

³⁷S. Paul, B. Bayha, W. Lerch, C. Merkl, D. F. Downey, and E. A. Arevalo, Proceedings of the 14th International Conference on Ion Implantation Technology, 2002, p. 83.

³⁸P. J. Timans, W. Lerch, S. Paul, J. Niess, T. Heulsmann, and P. Schmid, *Solid State Technol.* **47**(5), 35 (2004).

³⁹W. Skorupa, T. Gebel, R. A. Yankox, S. Paul, W. Lerch, D. F. Downey, and E. A. Arevalo, *J. Electrochem. Soc.* **152**, G436 (2005).

⁴⁰A. Mokhberi, L. Pelaz, M. Aboy, L. Marques, J. Barbolla, E. Paton, S. McCoy, J. Ross, K. Elliott, J. Gelpey, P. B. Griffin, and J. D. Plummer, *Tech. Dig. - Int. Electron Devices Meet.* **2002**, 879.

⁴¹K. B. Parab, S.-H. Yang, S. J. Morris, S. Tian, A. F. Tasch, D. Kamenitsa, R. Simonton, and C. Magee, *J. Vac. Sci. Technol. B* **14**, 260 (1996).

⁴²M. Y. L. Jung, R. Gunawan, R. D. Braatz, and E. G. Seebauer, *J. Electrochem. Soc.* **150**, G838 (2003).

⁴³Y. I. Nissim, A. Lietoila, R. B. Gold, and J. F. Gibbons, *J. Appl. Phys.* **51**, 274 (1980).

⁴⁴P. Timans, J. Gelpey, S. McCoy, W. Lerch, and S. Paul, *Mater. Res. Soc. Symp. Proc.* **912**, 3 (2006).

⁴⁵A. Florakis, D. Tsoukalas, I. Zergioti, K. Giannakopoulos, P. Dimitrakakis, D. G. Papazoglou, G. Bennisayag, H. Bourdon, and A. Halimaoui, *Nucl.*

- Instrum. Methods Phys. Res. B **253**, 13 (2006).
- ⁴⁶F. Torregrosa, C. Laviron, F. Milesi, M. Hernandez, H. Faïk, and J. Venturini, Nucl. Instrum. Methods Phys. Res. B **237**, 18 (2005).
- ⁴⁷T. Ito, T. Inuma, A. Murakoshi, H. Akutsu, K. Suguro, T. Arikado, K. Okumura, M. Yoshioka, T. Owada, Y. Imaoka, H. Murayama, and T. Kusuda, Jpn. J. Appl. Phys. **41**, 2394 (2002).
- ⁴⁸W. S. Yoo and K. Kang, Nucl. Instrum. Methods Phys. Res. B **237**, 12 (2005).
- ⁴⁹J. Borland, R. J. Hillard, A. Mineji, W. Krull, M. Tanjyo, and T. Walker, Solid State Technol. **49**(5), 47 (2006).
- ⁵⁰C. H. Poon, L. S. Tan, B. J. Cho, A. See, and M. Bhat, J. Electrochem. Soc. **151**, G80 (2004).
- ⁵¹J. A. Sharp, N. E. B. Cowern, R. P. Webb, K. J. Kirkby, D. Giubertoni, S. Gennaro, M. Bersani, M. A. Foad, F. Cristiano, and P. F. Fazzini, Appl. Phys. Lett. **89**, 192105 (2006).
- ⁵²S. Earles, M. Law, R. Brindos, K. Jones, S. Talwar, and S. Corcoran, IEEE Trans. Electron Devices **49**, 1118 (2002).
- ⁵³E. V. Monakhov, B. G. Svensson, M. K. Linnarsson, A. la Magna, M. Italia, V. Privitera, G. Fortunato, M. Cuscunà, and L. Mariucci, Appl. Phys. Lett. **87**, 192109 (2005).
- ⁵⁴J. Venturini, M. Hernandez, G. Kerrien, C. Laviron, D. Camel, J. L. Santtailler, T. Sarnet, and J. Boulmer, Thin Solid Films **453–454**, 145 (2004).